NNT : ***

n°LAL : ***

Thèse de doctorat

Search of the $0\nu\beta\beta$ decay with the SuperNEMO demonstrator

Thèse de doctorat de l'Université Paris-Saclay
préparée à l'Université Paris Saclay au sein du Laboratoire Irène-Joliot Curie
(anciennement Laboratoire de l'Accélérateur Linéaire)

École doctorale n°576 Particles, Hadrons, Energy, Nuclei, Instrumentation,
Imaging, Cosmos et Simulation (PHENIICS)
Spécialité de doctorat : Physique des particules

Thèse présentée et soutenue à Orsay, le ***, par

CLOÉ GIRARD-CARILLO

Composition du Jury :

***	
***	Président
***	
***	Rapporteur
***	
***	Rapporteur
Christine Marquet	
CENBG - Bordeaux-Gradignan	Examinateur
***	
***	Examinateur
***	
***	Examinateur
Laurent Simard	
LAL - Orsay	Directeur de thèse
Mathieu Bongrand	
LAL - Orsay	Co-directeur de thèse

Contents

Introduction

Chapter 1

Phenomenology of particle physics

1.1 The Standard Model of particle physics

1.1.1 Bosons

1.1.2 Fermions

1.1.3 $2\nu\beta\beta$ decay

1.1.4 Where the Standard Model ends

1.2 Going beyond the Standard Model with neutrinos

1.2.1 Neutrino flavors and oscillations

1.2.2 Neutrino masses and nature

1.2.3 Other searches beyond the Standard Model with neutrinos

Chapter 2

$0\nu\beta\beta$ experiment status

2.1 Experimental design criteria

As no neutrinos are emitted in a $0\nu\beta\beta$ decay, the minimal observable in direct searches for $0\nu\beta\beta$ decay is the total energy of the two emitted electrons. Depending on experiment designs and purposes (detailed in Sec. 2.2), individual electron energies and tracks also represent interesting observables. The signature of a $0\nu\beta\beta$ signal is an excess of events, compared to the expected background noise, in the total energy spectrum, near the $Q_{\beta\beta}$ released energy. How large is this peak depends on the energy resolution of the detector. Research for this signal involves optimising a *region of interest* (ROI), also depending on the energy resolution. The total number of events $N^{0\nu}$ occuring in the ROI and in the measurement time t, for a detector with an detection efficiency ϵ, using a source isotope of W atomic molar mass and a isotopic abundance, is defined as

$$N^{0\nu} = \ln(2)\frac{\mathcal{N}_A}{W}\left(\frac{a\epsilon Mt}{T^{0\nu}_{1/2}}\right), \tag{2.1}$$

where $\mathcal{N}_A$ is the Avogadro number. If no excess of events is observed, the limit set on the $0\nu\beta\beta$ decay half-life is

$$T^{0\nu,\text{lim}}_{1/2} = \ln(2)\frac{\mathcal{N}_A}{W}\left(\frac{a\epsilon Mt}{N_{\text{exc}}}\right), \tag{2.2}$$

N_{exc} being the number of $0\nu\beta\beta$ events excluded at a given confidence level in the ROI. Then, this sensitivity to the $0\nu\beta\beta$ decay would depend on the number of total counts in the ROI, some of them possibly being background events:

$$T^{0\nu,\text{lim}}_{1/2} \propto \begin{cases} aM\epsilon t & \text{if no background is expected,} \\ a\epsilon\sqrt{\frac{Mt}{B\Delta E}} & \text{with background.} \end{cases} \tag{2.3}$$

Here B is the background rate usually expressed in counts.keV^{-1}.kg^{-1}.y^{-1} (when normalised to the width of the ROI, the source mass, and the observation time) and ΔE is

the energy resolution. The advantage of a background free experiment clearly comes out: the $0\nu\beta\beta$ half life would increase linearly with the time of exposure t (as opposed to $\sqrt{t}$ for an experiment with a large number of background events). Then, it is clear that the control and the discrimination of background is of high priority for such $0\nu\beta\beta$ direct search experiments. We will discuss in Chap. 3 some important point to reduce the backgrounds for the $0\nu\beta\beta$ decay detection. Next to that, the previous expression fixes the choices that experimenters can make in designing a detector. An ideal isotope would have a high natural abundance and would be deployed with the higest mass possible in a detector with a high detection efficiency, a good energy resolution (small ΔE) under low-background conditions (small B). Of all the 35 isotopes capable of disintegrating through $2\nu\beta\beta$, none meets all the previous conditions. Expermimenters will then have to find compromises, which are at the origin of the different detection strategies. Detector can ether use an active or passive source. In the first case, the source is also the detection medium (detector technologies detailed in Sec. 2.2.1, 2.2.2 and 2.2.4). In the second case, the source is decoupled from the detection part of the experiment (see Sec. 2.2.3 and 2.2.5). In the next section, we provide a review of the current and future experiments that aim to discover the neutrinoless double beta decay.

2.1.1   Aspects of the nuclear matrix elements

2.1.2   Quenching

2.2 $0\nu\beta\beta$ direct search experiments

2.2.1   Semiconductors

Various semiconductor technologies are employed in the detection of $0\nu\beta\beta$ decay. The ^{76}Ge $\beta\beta$ emitter ($Q_{\beta\beta} = 2039$ keV) is historically important as it has been adopted since the 1960s in $0\nu\beta\beta$ decay searches, acting as active source, which enhances the detection efficiency. ^{76}Ge-enriched high purity Germanium detectors (HPGe) offer both high energy resolution and extremely high radiopurity (as impurities are removed in the crystal growing process). These characteristics allow, once external background contribution is minimised, to reach high sensitivity on $0\nu\beta\beta$ decay, which makes this category of detectors one of the most promising for ton-scale experiments. Since the last generation (IGEX and Heidelberg-Moscow), HPGe detectors had been improved to reach an ultra low background rate, making way for the current generation of $0\nu\beta\beta$ detectors – GERDA, MAJORANA demonstrator and LEGEND.

The **GERDA** experiment (GERmanium Detector Array) is located at the Laboratori Nazionali del Gran Sasso (LNGS), Italy. GERDA phase I was running from 2011 to 2013 with 17.8 kg of enriched active source detectors from the HEIDELBERG-MOSCOW and IGEX experiments. Its first aim was to put to the test the controversial result of

Experiment	Isotope	M (kmol)	$T_{1/2}^{0\nu}$ (90 % C.L.)	$m_{\beta\beta}$ (meV)
GERDA [1]	^{76}Ge	0.41	$9\,10^{25}$	$104 - 228$
MAJORANA [2]	^{76}Ge	0.34	$2.7\,10^{25}$	$157 - 346$
CUPID-0 [3]	^{82}Se	0.063	$0.24\,10^{25}$	$394 - 810$
CUORE [4]	^{130}Te	1.59	$1.5\,10^{25}$	$162 - 757$
EXO-200 [5]	^{136}Xe	1.04	$1.8\,10^{25}$	$93 - 287$
KamLAND-Zen [6]	^{136}Xe	2.52	$10.7\,10^{25}$	$76 - 234$

HEIDELBERG-MOSCOW experiment given in 2001, announcing the first evidence for $0\nu\beta\beta$ signal at a 4.2σ confidence level. With an exposure of 21.6 kg.y, the absence of signal in the GERDA-I experiment refuted the previous result, setting a limit $T_{1/2}^{0\nu} > 2.1\,10^{25}$ y. Since 2015, the GERDA experiment is in the second phase (see Fig. 2.1), with a total of 35.8 kg enriched detectors, 20 kg of which is Broad Energy Germanium (BEGe) detectors that have been deployed for GERDA-II, providing a better energy resolution and pulse shape discrimination. The active source is deployed inside a liquid Argon (LAr) augmented with light sensors, acting as an active external shield as well as a cooling down system. The total is surrounded by a water tank. The aim is to reach a 10^{26} y sensitivity with 100 kg.y exposure, and a background rate less than 10^{-3} counts.keV^{-1}.kg^{-1}.y^{-1}. The underground laboratory of INFN provides 3500 m water equivalent to reduce the external cosmic background. In 2019, a combined analysis for GERDA phases I and II has resulted in a half-life limit of $T_{1/2}^{0\nu} > 0.9\,10^{26}$ y (90% C.L., sensitivity assuming no signal is $1.1\,10^{26}$), corresponding to an effective neutrino mass of $m_{\beta\beta} < 0.07$-0.16 eV (90% C.L.)[1].

MAJORANA demonstrator
LEGEND

2.2.2 Bolometers

Bolometers are high energy resolution and high detection efficiency calorimeters operating at low temperatures ($\simeq 10 - 20$ mK). This type of detector is particularly suitable for $0\nu\beta\beta$ searches, with the possibility of building large-scale experiments.

CUORE
CUPID
AMoRE

---

[1]This result depends on the nuclear matrix elements used for the calculations. See Sec. 2.1.1.
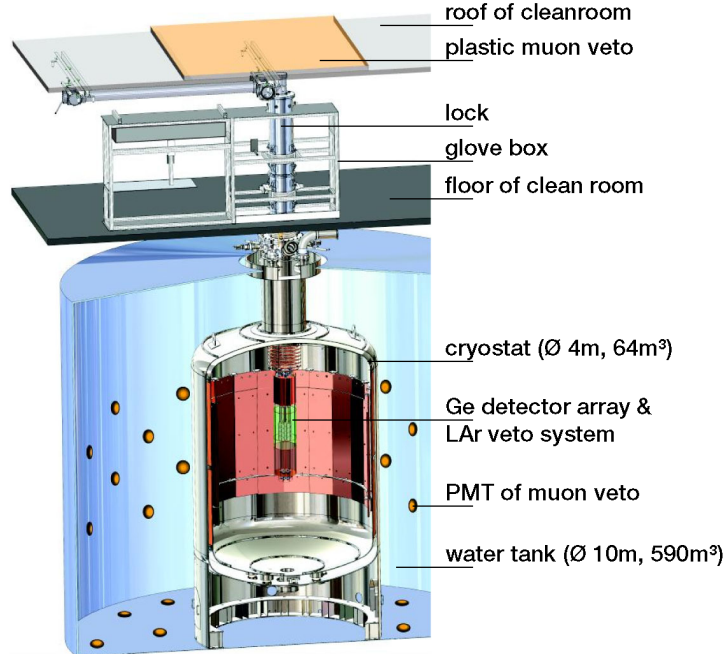
Figure 2.1

2.2.3   Time projection chambers

Time Projection Chambers (TPC) detectors use a medium producing two ways to measure
the electron energies: a *scintillation* (ultra-violet light) prompt signal, and a *ionisation*
delayed signal. When a particle crosses the detector, a scintillation light is emitted, the
energy of the scintillation peak depending on the medium. Scintillation photons, travelling
at speed of light in the medium, are detected by photosensors, giving the *zero-time* of the
event. The crossing particle ionises the medium all along its way, creating electrons drifting
to a collection system (an electric field is applied between cathode and anode), allowing
the precise measurement of the electron production location in a 2D plane. The drift time
measurement gives access to the third coordinate of the interaction point. Therefore, com-
bining the two consecutive signals allows precise position and energy reconstruction. An
discriminating observable is the ionisation-to-scintillation ratio (see Fig. 2.2) as it provides
particle discrimination between α particles (low ratio) and γ radiations and β particles
(high ratio). For $0\nu\beta\beta$ searches, ^{136}Xe-enriched isotope in liquid phase is used, offering
a maximal source density (more compact detecors) and a good position resolution. Un-
fortunately, the energy resolution is worse than that of the gas-phase TPCs detectors[2].

---

[2]Two-phase liquid-Xenon detectors are developed for Dark Matter searches and could be exploited for
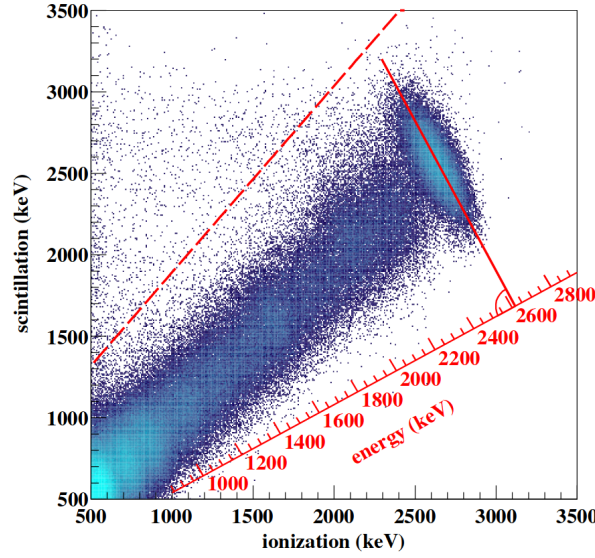$0\nu\beta\beta$ direct searches with the DARWIN project.

Figure 2.2

Noble elements are natural radiation detectors, avoiding the need for excess materials that could generate extra radioactive backgrounds. ^{136}Xe-enriched is the only noble element capable to $2\nu\beta\beta$ decay, with $Q_{\beta\beta} = 2457.8$ keV. This isotope has a relatively high natural abundance (9%), can be enriched to highly pure concentrations, and does not have other long-lived radioactive isotopes, making it interesting for large-scale TPCs $0\nu\beta\beta$ experiments.

The **EXO**-200 experiment is a prototype of the Enriched Xenon Observatory (EXO) project, currently operating in a room under an overburden of 1624 m.w.e, at the Waste Isolation Pilot Plant (WIPP), USA. The detector is shaped as a cylinder, with two back-to-back cylindrical TPCs. A high negative voltage grid cathode helds at the mid plane of the detector (40 cm diameter), and two anodes are located on both sides, at ground potential. A cross-section of the detector is displayed in Fig. 2.3. With 110 kg of enriched ^{136}Xe in liquid phase (the detector is held at 167 K in a cryogenic bath), the phase I of this TPC detector has measured for the first time the Xenon $2\nu\beta\beta$ decay with $T_{1/2}^{0\nu} = 2.165 \times 10^{21}$ y. Between phase I and IIa, the detector was upgraded with improved low-noise electronics, a Radon suppression system, and the impurities contents of the Xenon were reduced by a factor ten. The current detector performance shows an energy resolution of 2.90% (FWHM) at the decay Q-value and a background rate of $(1.6) \times 10^{-3}$counts.keV^{-1}.kg^{-1}.y^{-1}. EXO-200 phase IIa data placed a new limit of $T_{1/2}^{0\nu} > 1.8 \times 10^{25}$ y (90% C.L.). The final analysis of data is in progress.
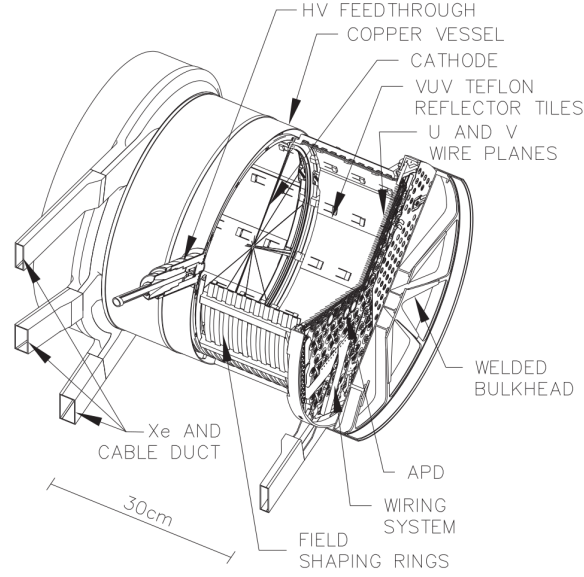
nEXO

Figure 2.3

NEXT
PandaX-III

2.2.4   Scintillators

KamLAND-ZEN and KamLAND2-ZEN
ZICOS
CANDLES

2.2.5   Tracking calorimeters

Tracking calorimeters technology, instead of using a *source-as-detector*, employ a passive source shaped as thin source foils of enriched $\beta\beta$ emitters. Sources are placed at the detector centre, surrounded by two trackers allowing for particle identification (between electrons, positrons, γ and α particles) and vertex reconstruction to improve the background rejection. The whole is sandwiched between calorimeters enabling individual particle energy reconstruction. In case of a discovery, this passive source tracking calorimeter technology provides topological information on angular emissions of the two electrons from $\beta\beta$ decay, making possible to distinguish between underlying mechanisms for $0\nu\beta\beta$ decay (see Sec. 1.2.2).

The **SuperNEMO** experiment is a next-generation of detector, inheriting the lineage of the NEMO (Neutrino Ettore Majorana Observatory) experiments, which successfully studied multiple isotopes as enriched Molybdenum ^{100}Mo.

Chapter 3

The SuperNemo demonstrator

3.1 The SuperNemo demonstrator

3.1.1 Comparison with Nemo3 experiment

3.1.2 Experimimental design

3.1.3 Sources

3.1.4 Tracker

3.1.5 Calorimeter

3.1.6 Calibration systems

3.1.7 Control Monitoring system

3.1.8 Electronics

3.2 The SuperNemo software

3.2.1 Simulation

3.2.2 Reconstruction

Chapter 4

Analysis tools

4.0.1 Internal probability

Internal probability is a mathematical tool used to quantify the probability that two particles (in this study only electrons will be considered) were emitted simultaneously and at the same location in the source foils. The internal probability is defined from the associated internal χ^2

$$\chi^2_{int} = \frac{((t_1^{exp} - \frac{L_1}{\beta_1 c}) - (t_2^{exp} - \frac{L_2}{\beta_2 c}))^2}{\sigma^2_{tot}} \, , \tag{4.1}$$

where c is the speed of light, t_i^{exp} is the time measured in calorimeters for the particle i, L_i is the reconstructed track length, and β_i is defined as $\sqrt{E_i(E_i + 2m_e)}/(E_i + m_e)$, E_i being the energy of particle i and m_e the electron mass.

The denominator in eq. 4.1 is the total uncertainty defined as

$$\sigma_{tot} = \sqrt{\sigma_t^2 + \sigma^2_{\left(\frac{L}{\beta c}\right)} + \sigma_l^2} \, , \tag{4.2}$$

where the first term $\sigma_t^2 = \sum_{i=1,2} \sigma^2_{t_i}$ is the uncertainty the time measurement in the calorimeters with σ_t defined as

$$\sigma_t = \sqrt{\frac{\tau^2_{\text{SC}} + \left(\frac{\text{FWHM(TTS)}}{2\sqrt{2\ln 2}}\right)^2}{\text{N}_{\text{PE}}}} \, . \tag{4.3}$$

The second term $\sigma^2_{\left(\frac{L}{\beta c}\right)} = \sum_{i=1,2} \sigma^2_{\left(\frac{L_i}{\beta_i c}\right)}$ is the uncertainty depending on the energy of electron i as

$$\sigma_{\left(\frac{L}{\beta c}\right)} = \left|\frac{\partial t_{th}}{\partial E}\right| \Delta E \, . \tag{4.4}$$

The third term σ_L represents the typical uncertainty due to track reconstructions of particles[1].

Then the internal probability evaluate the difference between experimentally measured time and theoretical times.

4.1   Simulations

4.1.1   Modifications of simulation software

4.1.2   Internal background simulations

4.1.3 $0\nu\beta\beta$ simulations

---

[1]This value is set to $\sigma_L = 0.03$ ns in a first approximation (see chapter -ref-).

Chapter 5

Time difference

The ultimate internal background for $0\nu\beta\beta$ experiments is the $2\nu\beta\beta$ decay of the studied isotope. Background due to contamination of ^{238}U decay chain. When present in the source foils, ^{208}Tl and ^{214}Bi can mimic the $0\nu\beta\beta$ signal by different processes (see Fig. 5.1). For this study, we are focusing on the internal conversion process coming from the contamination of ^{208}Tl in the source foils. Regarding the simplified desintegration scheme of the ^{208}Tl isotope (Fig. 5.2), we see that the β desintegration has 51% of probability to fall on the 294 ps-life time exited level. To decay to ^{208}Pb, the exited isotope has 100% of probability to decay emmiting a γ of 2.6 keV. In 0.2% of cases, one of the orbital electron can interact with the exited nucleus and decay through internal conversion. To summarise, decays where a ^{208}Tl nucleus emmits a β particle and then an electron comming from internal conversion of the 2.6 MeV-γ represents 75% of the total β decays. In this case, the internal conversion electron is time-delayed of 294 ps compared with the β particle. We aim to use this delayed electron to discriminate ^{208}Tl internal background from signal and other internal backgrounds.

5.1 Principle and goal

5.1.1 Internal conversion

Despite its name, internal conversion has nothing to do with the internal probability. Internal conversion occurs after β or α radioactive decays leaving the nucleus exited. Then a γ particle is emitted and transfers its energy to an atomic electron which results in ejection of this electron from the atom. The emitted electron has an energy corresponding to the energy of previously exited nucleus reduced by the electron binding energy. After the internal conversion, electrons reorganise. The hole in internal layer is filled by an electron from an external layer (emitting an X ray).

The probability for an atomic electron to be ejected decreases with the initial binding
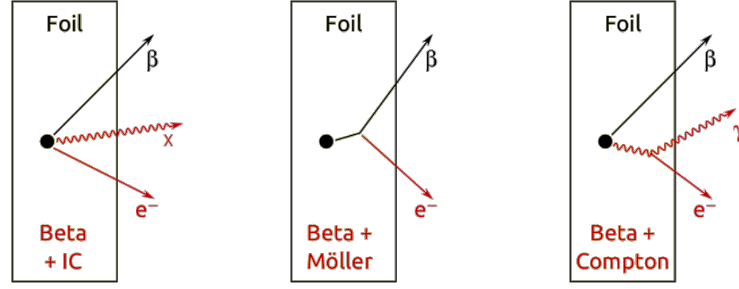
Figure 5.1: (a) β decay + internal convertion: ^{208}Tl nucleus performs a β decay, then an electron is emitted after internal conversion of photon (b) β decay + Möller: (c) β decay + Compton diffusion: ^{208}Tl nucleus β decays to an exited state, then the photon perfoms a Compton diffusion.

energy. Thus, electrons from K layers have a higher probability to be converted (see Fig. 5.3).

5.2   Analysis

5.2.1   Topological cuts

5.2.2   Exponentially modified Gaussian
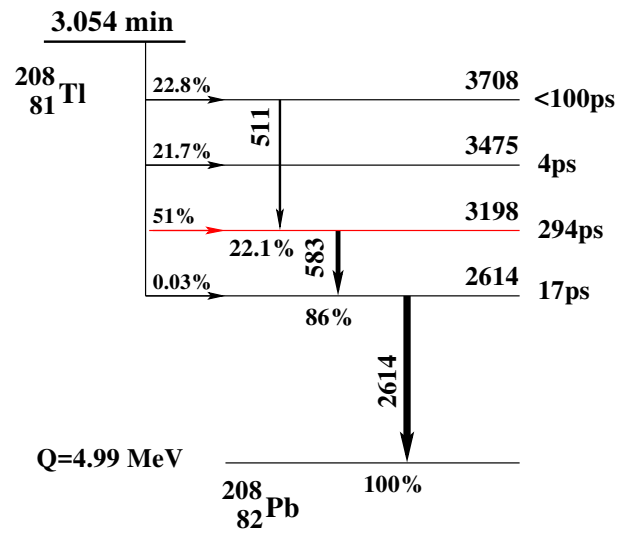
5.2.3   Results

5.3   Conclusion

Figure 5.2: Simplified desintegration scheme for ^{208}Tl isotope. The level in red has a significant life time of 294 ps and can be useful in internal backgroung rejection.
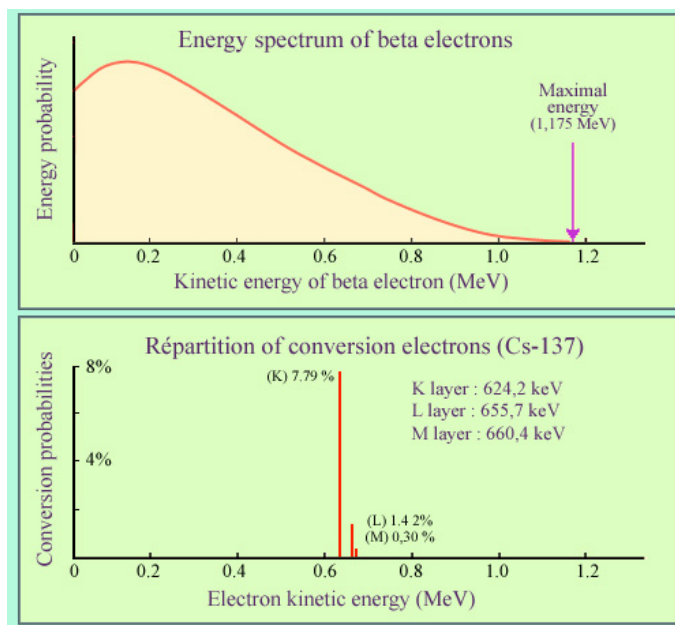

Figure 5.3

Chapter 6

Detector commissioning

The commissioning of the SuperNEMO demonstrator has begun in 2019 and first calorimeter data was taken.

The calorimeter of SuperNEMO is segmented in 712 optical modules (OM), each composed by a coupling between a photomultiplier tube (PMT) and a polystyrene scintillator bloc (see sec. 3.1.5 for more details). The divider of a PMT is connected to 2 cables, one providing the high voltage (HV), the other one, called signal cable, is a coaxial cable collecting and transporting the charge provided by the PMT.

By the summer 2020, the SuperNEMO demonstrator will be encapsulated in an anti radon tent. The so called *patch panel* will insure passage of cables from the inside, to the outside of the anti radon tent, therefore doubling the amount of cables needed for the calorimeter. We refer to the cables running from detector to patch panel as *internal* cables, and the cables from patch panel to the electronic boards as *external* cables. Consequently, regarding only the calorimeter part, 2848 cables were cut, assembled, connector-mounted, transported and installed at LSM. Then the check of every cable condition is mandatory to control and eventually fix them.

6.1   Reflectometry analysis

6.1.1   Goal of the reflectometry analysis

Taking into account the final demonstrator design, each coaxial length was determined, cables were cut and labelled in LAL, Orsay. All external coaxial cables were designed to be 7 meters-long – the distance between electronic boards and patch panel being the same for all channels at electronic boards – and internal cable lengths have been adapted to fit the distance from the patch panel to each optical module. Then, cutting and labelling all cables lasted several weeks. After all cables were transported and installed at LSM, we had to check each coaxial cable condition, for several reasons:

27

(a) Normal reflection at   (b) Cable not connected at   (c) Cable not connected at
    PMT divider.   PMT.   patch panel.
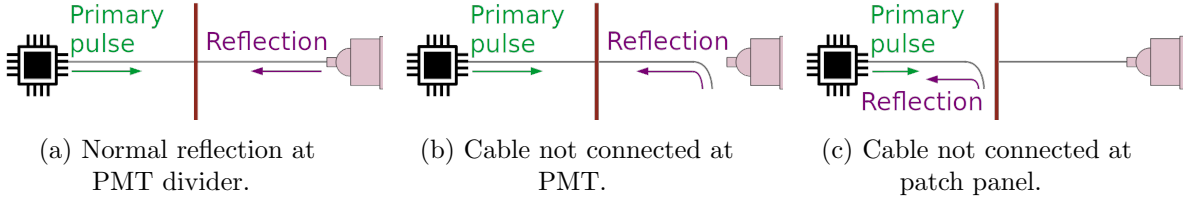
Figure 6.1: A representation of pulses sent in a cable for the reflectometry analysis is given. The electronic boards are symbolised by the black chip, and the patch panel by the red vertical bar. Three scenario where a primary pulse is sent in one cable (represented in grey), are represented. (a) The cable is well connected at the patch panel and at the PMT. The signal reflects at the PMT divider. (b) The cable is not connected at PMT and the signal is reflected at the end of the cable. (c) The cable is not connected at patch panel and the signal is reflected at the end of the external cable.

- check if no cable was damaged during the transport and the installation;

- control if no swap between cables has been made during cable labelling or calorimeter cabling,

- check if the coaxial cable was cut at the right length,

- more importantly estimate the signal time delay due to the cable lengths: knowing that the velocity of electrons in the coaxial cables has a known constant value, the longer is the cable, the more the signal takes time to travel from the PMT to the electronic channel. Therefore, each coaxial cable length has to be characterised, especially if we want to do time coincidences between two signals in two different channels.

To do so, a pulse, called *primary* pulse, is generated at the electronic board readout. The signal will travel all along the coaxial cable, from the electronic board to the PMT divider. Whether the cable is correctly connected to the PMT or not, the signal reflects at the other end. Then the signal travels back from the PMT to the electronic board channel, where it is recorded by the acquisition. We called this recorded reflected pulse *secondary* pulse. An example of the total recorded signal is displayed in Fig. 6.3. In order to accumulate enough statistics, we send thousands of pulses in each coaxial cable. The analyses of the shape and of the arrival time of those secondary pulses for each channel is called *reflectometry*, and allow us to check the coaxial cable conditions and to control their lengths.

6.1.2   Pulse timing: controlling cable lengths

The first step of this analysis is to experimentally determine the length l_j^m for all signal cables j installed on the demonstrator. This length is defined as

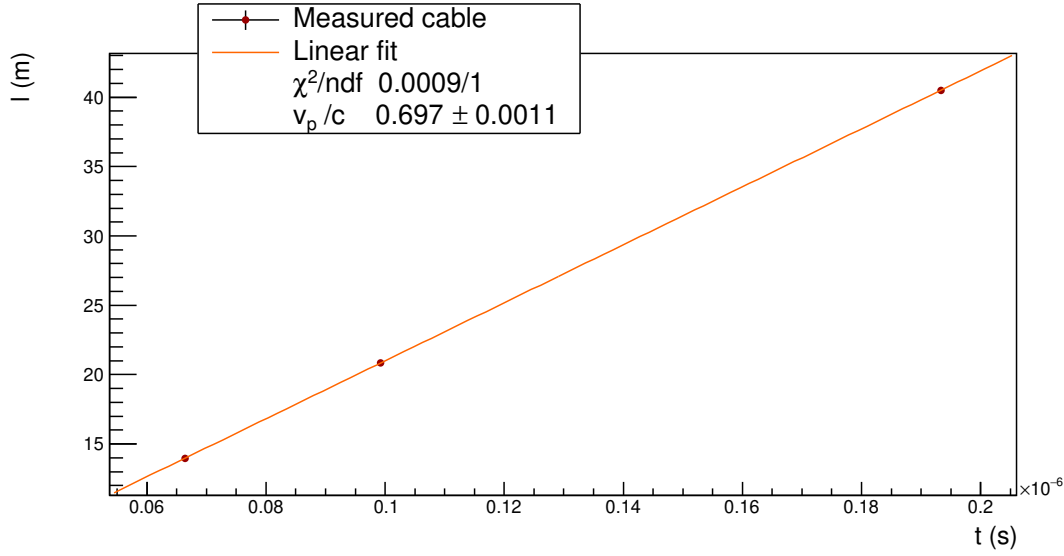$$l_j^m = 0.5\, t_j\, v_p\,, \tag{6.1}$$

Figure 6.2: Three different lengths l_j of cables are measured. Pulses are sent inside all cables. The lengths l_j are plotted as a function of the time differences t_j between primary and secondary pulses. The value of v_p/c fitted from the data points is displayed. This value of 0.697 ± 0.0011 shows the compatibility with the one supplied by the constructor, of 0.69 c.

where t_j stands as the time made by the electrons to do a round trip between one electronic channel and one PMT, and v_p is the velocity of electrons in the coaxial cables, which can be expressed as a fraction of light speed in vacuum, c. The time difference t_j between the primary pulse and the secondary pulse is written as

$$t_j = \langle t_{\text{secondary pulse}} - t_{\text{primary pulse}} \rangle_p \,, \tag{6.2}$$

$\langle \rangle_p$ being the average over all pulses sent in one single cable j. The velocity v_p is supplied by the cable manufacturer as

$$v_p = \frac{c}{\sqrt{\epsilon_r}} \,,$$

with ϵ_r the relative dielectric constant of the material. Therefore, this celerity depends on the components. For the coaxial cables chosen in the demonstrator design, the data sheet of the cable gives $v_p = 0.69\,c$. A study is performed to verify experimentally the value of v_p. Three cables of different lengths are measured with a precision of 1 cm. A thousand of primary pulses are sent in each of the three cables, then the time for each secondary pulse is recorded. At the end, we have three independent measures of the velocity v_p in the used coaxial cables. On Fig. 6.2 is displayed the lengths l_j as a function of the times t_j. The fitted value of $v_p/c = 0.697 \pm 0.0011$ is displayed and shows a compatibility up to 7σ with the data sheet.
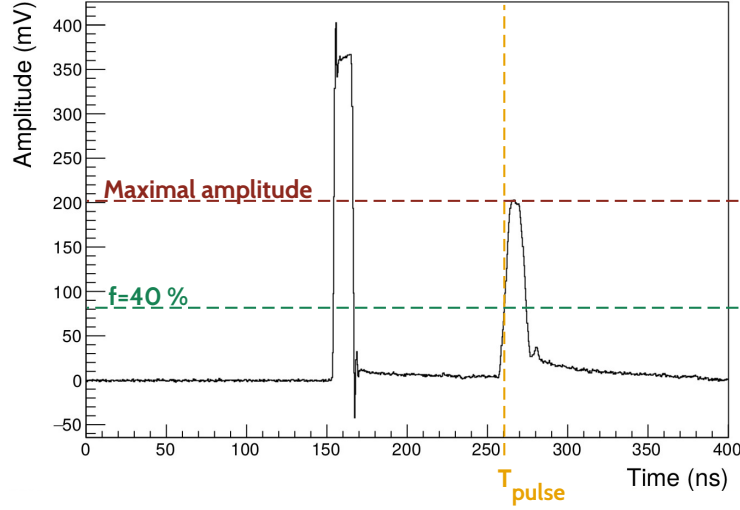
Figure 6.3: In black is shown an example of a total recorded waveform with the primary pulse (left) and secondary the pulse (right). A representation of time computed with a Constant Fraction Discriminator (CFD) is provided for the secondary pulse. Its maximal amplitude (red dotted line) and its fraction for f = 40% (green dotted line) are displayed. The time T_{pulse} (orange dotted line) represents the time of arrival of the secondary pulse computed with CFD, with the fraction f = 40%.

As we want to determine the time interval t_j, we have to define what is the *time* of a pulse. In this analysis, we use a technique called Constant Fraction Discriminator (CFD), providing an amplitude-independent information about time of a pulse. This algorithm aims at tracking a signal and defining its time arrival at a given fraction f of its maximal amplitude. The two main advantages of this technique is that it provides an efficient rejection of the noise in the acquisition window, and gives a good resolution on the measured time. Nevertheless, the possible influence of the chosen value for the f parameter on this time resolution has to be investigated. We perform such a study in Sec. **??**. We concluded that the highest precision on the time measurement arises for $f = 40\%$, and we adopt this value for the following analysis. A graphic representation of the CFD time search is given in fig. 6.3.

As we want to measure the installed cable lengths l_j^m, and compare them to the initially designed ones, l_j^d, we define the length difference ΔL_j as:

$$\Delta L_j = l_j^m - l_j^d. \tag{6.3}$$

On Fig. 6.4 is displayed the distribution ΔL for all the measured lengths. In hypothetical perfect conditions, all the cables should fit the design length, in other words, $l_j^d = l_j^m$. Consequently the ΔL distribution should a peak at zero, as materialised by the black
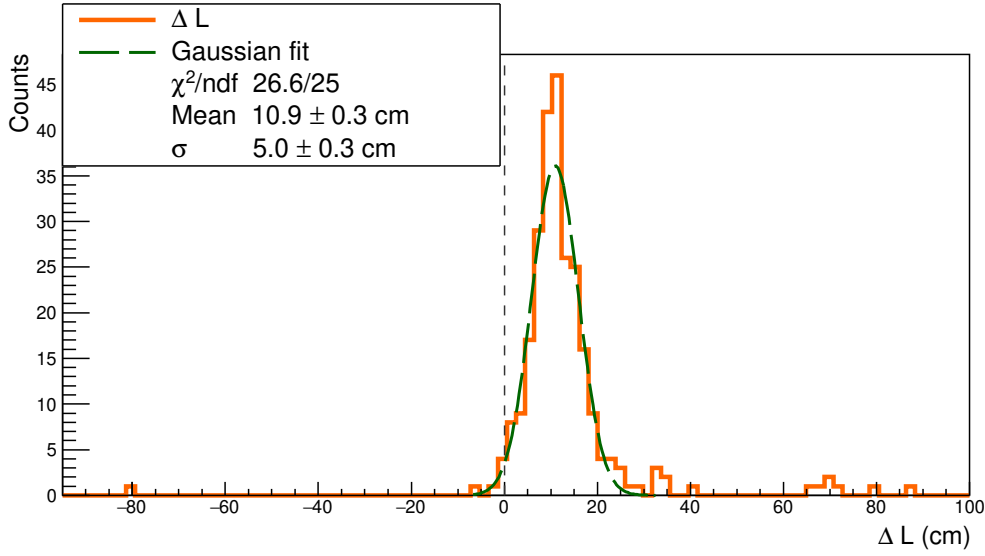
Figure 6.4: The distribution of difference between the measured lengths l^m and the expected lengths l^d is displayed in orange plain line. The black dashed line represents the case where $l_j^m = l_j^d \ \forall j$. The Gaussian fit (green dashed line) presents a mean of 10.9 ± 0.3 cm. Some data points considered as outliers are beyond 3σ.

dashed line. However, in real conditions, the measured length can be different from the designed one, leading the ΔL distribution plotted in orange plain line. We conclude that the observed cable length l^m differs from l^d by $+10.9 \pm 0.3$ cm, meaning that cables are longer than expected in average. This may reveal a bias coming from the device used to cut the cables. In fact, during cable cutting work, we noticed that the cutting device had a tendency to slip, probably leading to cables with extra lengths. We assumed the cutting device has a given probability to slip for one meter of cable. If this is the case, the probability for the device to give extra length should increase with the cable length.

To verify this assumption, we plot on Fig. 6.5 the length difference ΔL as a function of the initial design length l^d (cyan). From those data points, we compute a linear fit (orange plain line), parameterised as $y = \alpha x + \beta$, revealing that the cutting device presents two different biases. The value of β shows that the cutting device systematically took away 3.4 cm of each cable. Nevertheless, as the shortest cable was designed to be 10 meters long, there are no important consequences of this bias on the length difference ΔL. Besides, the slope $\alpha = 0.010 \pm 0.002$ of the linear fit reveals that the cutting device adds one centimetre for every meter of cable, being compatible with the hypothesis on the cutting device sliding. Hopefully this bias is not problematic as it makes most of the actual cable lengths longer than the design, while shorter lengths could have lead to systematic connection issues to PMTs. However, we notice that a few cables have been cut too short
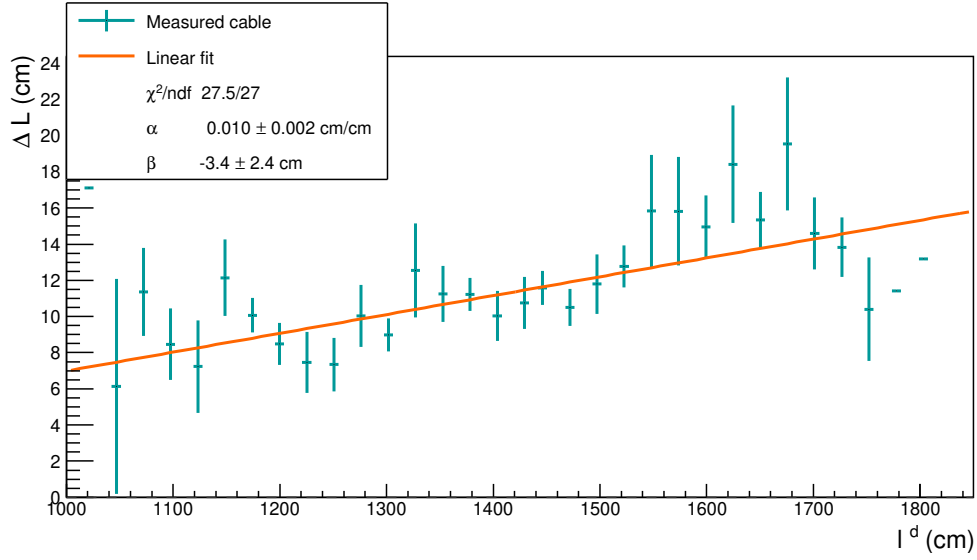
Figure 6.5: ΔL is plotted with l^d (cyan), where l^d is averaged for all the lengths designed to have the same value, being at the origin of vertical error bars. In black dashed line is represented the case where $l^m = l^m$. Data points are fitted by $\alpha x + \beta$, with $\alpha > 0$ and $\beta < 0$, revealing the two biases of the cutting device.

by mistake, the worse of them being 80 centimetres shorter than expected. Fortunately, this cable was successfully connected to PMT despite this deficit. On the contrary, few cables have a large extra length. This probably is due to human punctual mistakes on top of the observed bias, but without any strong consequences for the calorimeter operation. In conclusion, no important mistakes have been made when cutting cables, and we had no issue for connecting the only problematic cable.

If the main goal of this study is to check the lengths of coaxial cables, it also aims at correcting the time of recorded events, from the time made by the signal to travel from a PMT to an electronic channel. taking into account the time for the signal to travel through cables. This become possible with the reflectometry study we performed. Knowing real lengths of cables and using the celerity of the signal, we deduce the time needed for the signal to travel from one given PMT divider to the electronic boards. Then we can correct event times.

As explained previously, the time t_j gives information about the length of the cable j. We remind the coaxial cables are divided in two parts, one external and one internal, both linked by the so-called patch panel. Thus we can use that travel time to detect possible disconnection of a cable at patch panel. In fact, if one cable is not connected at the patch panel – this case is illustrated in Fig. 6.1c, – the pulse reflects at the end of the external cable part, going back to the electronic board. This very short time, giving information

about the location of the reflection, is used to tag a patch-panel disconnection. Then, a simple check onsite can confirm this observation, and the external part of the cable can be connected to the patch panel.

This study allowed us to control and record the lengths of all coaxial cables installed on the SuperNEMO demonstrator at LSM, and gave information on the status of cable connections at patch panel. We also have understood the main results on measured cable lengths and the functioning and biases of the cutting device that we used.

6.1.3 Signal attenuation

The attenuation of an electric signal is a problem common to all electronic fields, and comes from the charge loss of an electromagnetic wave travelling in a medium. For a coaxial cable, this attenuation mainly depends on the signal frequency f in MHz and on the cable characteristics. For the coaxial cables, the theoretical linear attenuation $\alpha_{\text{att}}^{\text{th}}$, so be it the attenuation by metre of cable in dB/m, is supplied by the constructor as

$$\alpha_{\text{att}}^{\text{th}} = f \sqrt{\epsilon} \left(\frac{a}{\sqrt{f}} + b \right), \tag{6.4}$$

where the factor a depends on the diameter of the dielectric material on one hand, and of the diameter of the conductor material on the other hand, and where b is function of the dielectric loss factor, characterising the material's dissipation of electromagnetic energy. For the used coaxial cables, and with a frequency f of few GHz for the signal pulses sent in cables, we calculate this attenuation as $\alpha_{\text{att}}^{\text{th}} = 1.22$ dB/m. In a more general manner, the attenuation of a signal in dB is defined with the decimal logarithm of a power ratio. We use this definition to determine the attenuation in the framework of the reflectometry analysis, defining the attenuation $\mathcal{A}$, for a given length of cable l, as

$$\mathcal{A} = 10 \log_{10} \frac{V_{\text{primary pulse}}}{V_{\text{secondary pulse}}}, \tag{6.5}$$

where V_i is a quantity representing the intensity of the signal. V can correspond to the maximal amplitude of the pulse, as well as the *integrated charge* of the pulse, defined as the amount of current received by the acquisition over a given time window. As the provided data sheet does not specify the attenuation of which quantity (amplitude or charge) represents $\alpha_{\text{att}}^{\text{th}}$, we decide to investigate both in the following. Then, we define the linear attenuation $\alpha_{\text{att}}^{\text{R}}$, measured by reflectometry in dB/m, with

$$\mathcal{A} = f_r + \alpha_{\text{att}}^{\text{R}} \, l, \tag{6.6}$$

with $f_r = -10 \log_{10} R$, where R is the reflection factor characterising the pulse reflection on the PMT divider. In fact, as the circuit is opened, the pulse is reflected at the PMT

divider, but only partially. A part of the signal is not reflected but lost through the divider. This reflection is characterised by R, which is function of the impedance Z_c of the cable, and of the impedance Z_d at the divider level, where the pulse is reflected. It is written as

$$R = \frac{Z_d - Z_c}{Z_d + Z_c} \,, \tag{6.7}$$

where we have the limit

$$\lim_{Z_d \to \infty} f_r = 0 \text{ and } R = 1 \,, \tag{6.8}$$

expressing a total reflection occurring when the impedance at the PMT divider is infinite. The main goal here is to determine the value of $\alpha_{\text{att}}^{\text{R}}$, using the reflectometry data, and to compare it with $\alpha_{\text{att}}^{\text{th}}$. Moreover, the impedance Z_d value at PMT divider can be estimated from the determination of f_r. On Fig. 6.6 is shown the linear dependence between the attenuation $\mathcal{A}$ and the cable length l, and two data set are presented. The cyan scattered markers represent the attenuation calculated from the amplitude ratio $A_{\text{primary pulse}}/A_{\text{secondary pulse}}$, and the magenta markers correspond to the attenuation calculated from the charge ratio $Q_{\text{primary pulse}}/Q_{\text{secondary pulse}}$. The amplitude A_i is given in mV and the charge Q_i in mV.ns. The values of $\alpha_{\text{att}}^{\text{R}}$ and f_r, for both amplitude and charge cases, are displayed in the legend. Firstly, the two linear fits reveal that, whether calculated with the amplitude, or with the charge, the linear attenuation $\alpha_{\text{att}}^{\text{R}}$ is smaller than the calculated one $\alpha_{\text{att}}^{\text{th}}$ (for the amplitude case, $\alpha_{\text{att}}^{\text{th}} \simeq 5 \times \alpha_{\text{att}}^{\text{R, amp}}$, and for the charge case $\alpha_{\text{att}}^{\text{th}} \simeq 7 \times \alpha_{\text{att}}^{\text{R, ch}}$). That means the signal is less affected, when transmitted by the cable, than expected. Secondly, the attenuation in charge is less important that the attenuation in amplitude. This can be easily explained: as it is integrated over time, the charge is a quantity less affected by amplitude variations that the amplitude itself. For the same reason, the charge data set points are less spread than the amplitude ones, meaning that we are less sensitive to cable length variations when using the charge quantity.

This work achieved, we want to verify if no cable was damaged after installation. Reflectometry also aimed at checking cable conditions by performing waveform shape analysis on secondary pulses.

6.1.4   Pulse shape analysis

On Fig. 6.3 is displayed an example of *normal* pulse, which corresponds to the case represented in Fig. 6.1a. In this case, the pulse sent in the cable travels to the PMT, and goes back to the acquisition after reflection on the divider.
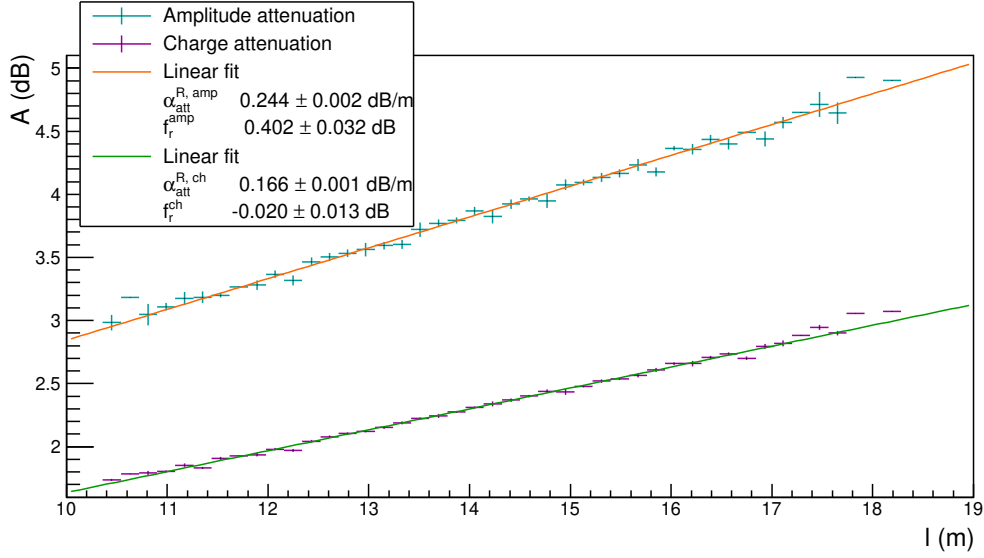
Figure 6.6: The amplitude $\mathcal{A}$ is displayed as a function of the measured cable length l. The data set calculated with the amplitude (charge) is given in cyan (magenta) and fitted by a linear function in orange (green). The values of the slope, which represent the linear attenuation of the coaxial cables in dB/m, are respectively $\alpha_{\mathrm{att}}^{\mathrm{R,\ amp}} = 0.241 \pm 0.000\,\mathrm{dB/m}$ and $\alpha_{\mathrm{att}}^{\mathrm{R,\ ch}} = 0.166 \pm 0.000\,\mathrm{dB/m}$. The two y-intercept values, which represent the reflection of the pulse on the PMT divider, are $f_r^{amp} = 0.402 \pm 0.032$ dB and $f_r^{ch} = -0.020 \pm 0.013$ dB.

6.1.5 Comparison with ^{60}Co

6.2 Calibrating the electronic boards

6.2.1 Principle

6.2.2 Measuring the time offset of front end boards

6.2.3 Results

Chapter 7

Characterisation of the calorimeter resolution

Optical modules have been characterised before installation. Most of the ^{60}Co β disintegration are followed by the emission of two γs in coincidence (see Fig. 7.4). The idea is to use this source to calibrate in time optical modules of SuperNEMO demonstrator by placing it behind the main calorimeter walls (the demonstrator being closed since ...) and using the two coincidence γs. Performing simulations of ^{60}Co disintegration

7.1 Calibration with a Cobalt source

7.1.1 Experimental setting and goal

7.1.2 Data taking at LSM

7.1.3 Analysis

7.1.4 Results

7.2 The Light Injection System

The SuperNEMO demonstrator is designed to have a long exposure time. In this context, calibration systems are necessary to control and calibrate the response of the detector. The so called *Light Injection* (LI) System will monitor the stability of the calorimeter response in energy to 1%. It consists in 20 Light Emitting Diodes (LED) at 385 nm, injecting light in each scintillator block via optical fibers. A set of reference optical modules (PMTs coupled with scintillator blocks), receiving light from both LEDs and ^{241}Am sources, monitors the stability of the LEDs. A scheme of the complete LI calibration system is given in Fig. 7.1.

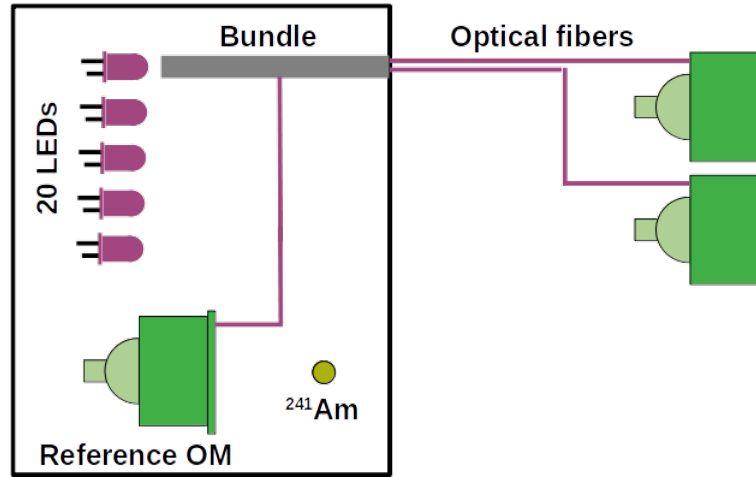First LI commissioning data was taken in March 2019.

Figure 7.1: The Light Infection (LI) calibration system is schematised. More than 1300 fibers, distributed in 20 bundles, carry the light from 20 LEDs to each scintillator block of the demonstrator. Reference OMs coupled with ^{241}Am sources monitor the LED light.

7.2.1   Light injection system commissioning

In the LI system design, the SuperNEMO demonstrator has been segmented in 10 areas. Each area receives light from one given LED

Primary/secondary Each LED lights Group LEDs/area

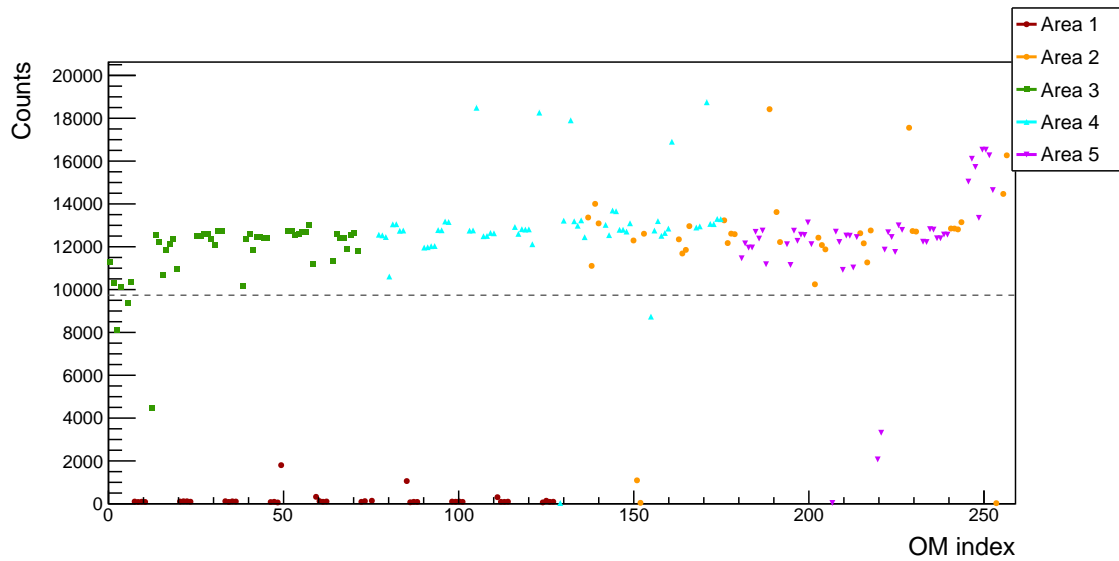### 7.2.2   Time resolution of optical modules

Figure 7.2: The number of counts is displayed for each optical module, labeled by the *OM index*. Each coloured marker represents counting rates for one area of the detector, that is to say one group of optical modules lighted by the same LED. The area #1 (dark red dots) is not receiving light from its coresponding LED.
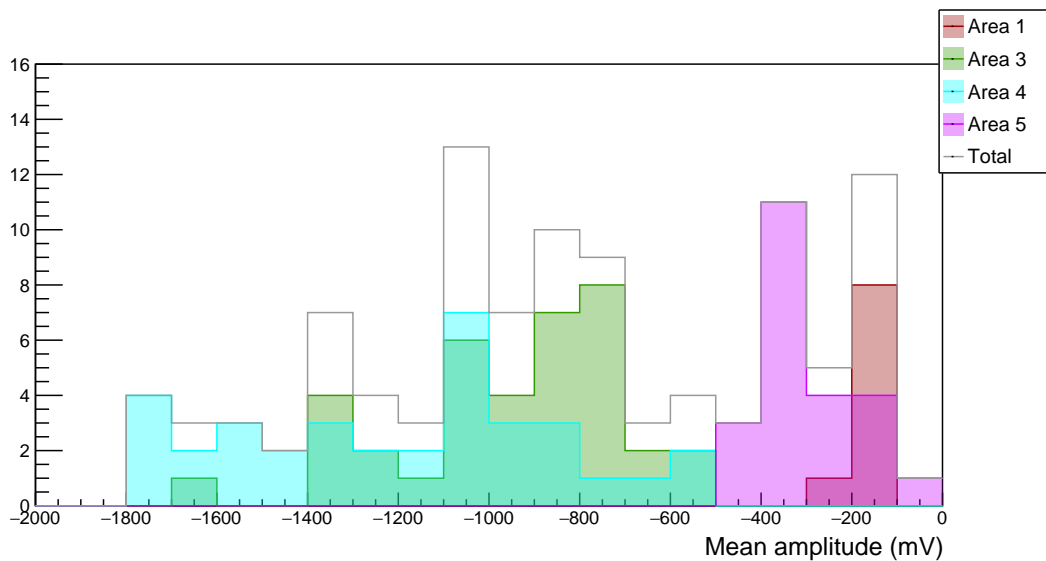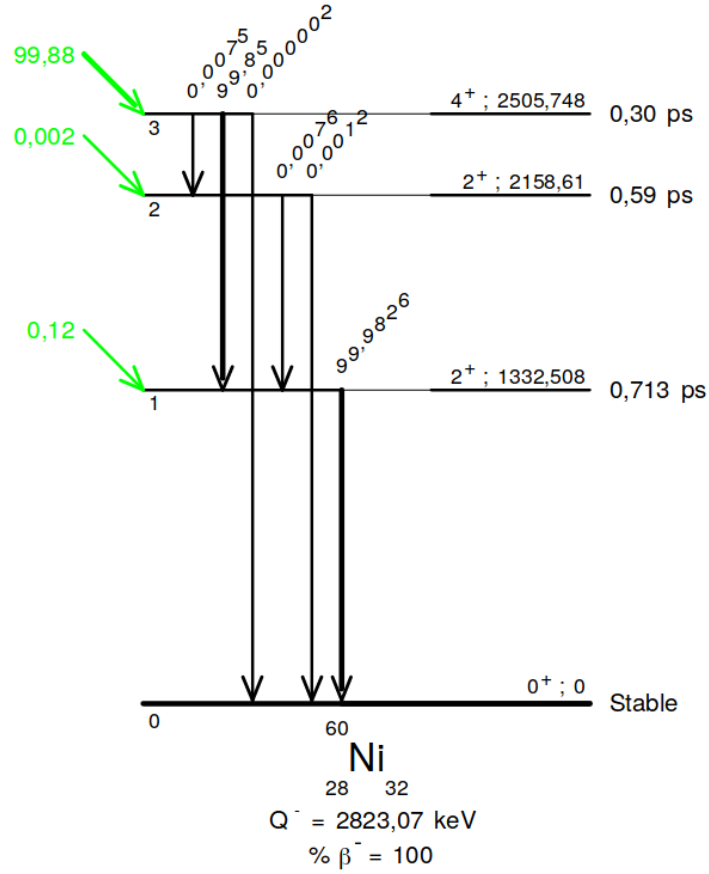

Figure 7.3: The mean signal amplitude distribution for each optical module is presented. One colour stands for one area of the half detector. In Grey is the total mean amplitude distribution.

Figure 7.4: Decay scheme of Cobalt 60. After the β disintegration 99.88%,

Conclusion

Bibliography

[1] M. et al. Agostini. Probing majorana neutrinos with double-β decay. *Science 365*, 1445, 2019.

[2] S.I. et al Alvis. Search for neutrinoless double-beta decay in ^{76}ge with 26 kg-yr of exposure from the majorana demonstrator. *Phys. Rev. C*, 100, 2019.

[3] O. et al. Azzolini. First result on the neutrinoless double-β decay of ^{82}Se with cupid-0. *Phys. Rev. Lett.*, 120:232502, Jun 2018.

[4] C. et al. Alduino. First results from cuore: A search for lepton number violation via $0\nu\beta\beta$ decay of ^{130}Te. *Phys. Rev. Lett.*, 120:132501, Mar 2018.

[5] J. B. et al. Albert. Search for neutrinoless double-beta decay with the upgraded exo-200 detector. *Phys. Rev. Lett.*, 120:072701, Feb 2018.

[6] A. et al. Gando. Search for majorana neutrinos near the inverted mass hierarchy region with kamland-zen. *Phys. Rev. Lett.*, 117:082503, Aug 2016.